SAND2021-14984C

Verification Studies of the Multi-Fidelity Toolkit

Aaron M. Krueger*, Blake W. Lance†, Brian A. Freno‡, and Ross M. Wagnild§
Sandia National Laboratories, Albuquerque, NM, 87123

The Multi-Fidelity Toolkit (MFTK) is a simulation tool being developed at Sandia National Laboratories for aerodynamic predictions of compressible flows over a range of physics fidelities and computational speeds. These models include the Reynolds-Averaged Navier–Stokes (RANS) equations, the Euler equations, and modified Newtonian aerodynamics (MNA) equations, and they can be invoked independently or coupled with hierarchical Kriging to interpolate between high-fidelity simulations using lower-fidelity data. However, as with any new simulation capability, verification and validation are necessary to gather credibility evidence. This work describes formal code- and solution-verification activities. Code verification is performed on the MNA model by comparing with an analytical solution for flat-plate and inclined-plate geometries. Solution-verification activities include grid-refinement studies of HIFiRE-1 wind tunnel measurements, which are used for validation, for all model fidelities.

I. Introduction

The Multi-Fidelity Toolkit (MFTK) is a suite of tools being developed at Sandia National Laboratories to improve the response time for aerothermodynamic queries for hypersonic flight vehicles. The toolkit comprises three levels of aerothermodynamic physics fidelity and a series of file- and data-processing scripts: an input-file generator, a sample-point dispatcher, a data-gathering code, and a multi-fidelity interpolation code. The aerothermodynamic evaluation fidelity levels are being developed in the Sandia Parallel Aerodynamics and Reentry Code (SPARC) and consist of a modified Newtonian aerodynamics (MNA) solver, an Euler solver, and a Reynolds-Averaged Navier–Stokes (RANS) solver. The low- and medium-fidelity models do not have the ability to compute viscous effects such as heat flux; therefore, both transfer data to different correlation-based models. The multi-fidelity interpolation code uses a hierarchical Kriging method [1] to perform sample evaluations over a parameter space by using trends from lower-fidelity predictions and anchoring to high-fidelity predictions, such as those from a RANS solver. This allows for more accurate predictions to be computed over a large parameter space at a reduced cost, compared to running a RANS solver only. With the multi-fidelity interpolation method, the focus of the lower-fidelity methods is on minimizing the error in the trend of aerothermodynamic data rather than the absolute error of each model. However, achieving the expected order of accuracy is necessary to ensure the lower-fidelity models have been correctly implemented.

To assess the credibility of predictions using MFTK, verification and validation activities are performed to ensure the correct implementation and appropriate use of the models. Validation assesses how well the implemented models represent the relevant physical phenomena. This is typically done by comparing simulation predictions with experimental data to assess the modeling error and ultimately the bounds of validity for a defined application space. By contrast, verification is, according to the American Society of Mechanical Engineers (ASME) Standard for Verification and Validation in Computational Solid Mechanics [2], “the process of determining that a computational model accurately represents the underlying model and its solution.” Verification is further broken up into code verification and solution verification [3–5]. Code verification focuses on the correct implementation of the mathematical model, whereas solution verification focuses on estimating the numerical error for a particular solution.

Previous work on the underlying models includes code verification of the Euler equations [6] and code and solution verification of the laminar equations [7]. To continue this effort, this paper focuses on code verification of the MNA model and solution verification of all the models in MFTK. When solving the underlying equations numerically, the geometry is discretized over the surface of the body. One consequence of discretizing the geometry is that the solution incurs a truncation error, which introduces a discretization error into the solution. By refining the mesh for a problem with a known solution and measuring the corresponding decrease in the discretization error, we compute an observed

---

[*] Senior Member of the Technical Staff; V&V, UQ, and Credibility Processes Department; Corresponding Author: amkrueg@sandia.gov
[†] Senior Member of the Technical Staff; V&V, UQ, and Credibility Processes Department; AIAA Member
[‡] Senior Member of the Technical Staff; V&V, UQ, and Credibility Processes Department; AIAA Senior Member
[§] Principal Member of the Technical Staff; Aerosciences Department; AIAA Senior Member

order of accuracy and compare it to the theoretical order of accuracy. When the comparison is sufficiently close, the likelihood of coding errors existing within the code is greatly reduced.

For solution verification, the exact solution is unknown. Therefore, we estimate the discretization error using the grid convergence index (GCI) metric [8]. GCI uses the difference between the Richardson extrapolated solution and the solution on the finest mesh as an approximation of the discretization error. To account for uncertainty within the calculation, the GCI metric applies a factor-of-safety multiplier to the estimated discretization error to account for errors not captured in the Richardson extrapolation calculation. The GCI metric is then applied as a bound on both sides of the solution on the finest mesh. Additional solution-verification methods exist [9–11], but these methods can be unnecessarily complex for simple problems.

II. Code Verification

Code verification is the first credibility activity to be completed for MFTK. This is done to ensure that coding errors are removed before impacting solution-verification or validation activities. The code-verification activities for this report focus on verifying the MNA model within MFTK. The MNA model is the inviscid component of the low-fidelity model within MFTK. In conjunction with a viscous component, such as the flat-plate boundary layer (FPBL) model, MFTK computes surface quantities for hypersonic flow calculations. MNA falls under the umbrella of local surface inclination methods. It is an improvement on Newtonian theory by accounting for the freestream Mach number when computing the coefficient of pressure [12]. Newtonian and MNA methods solve for the pressure coefficients, which in turn, allow for solving the surface pressure distribution. This method assumes parallel streamlines directed towards a surface. In the presence of a surface, such as an inclined plane, the fluid creates a pressure on the surface. While this model does not perform well for low-Mach flow, it has the potential to accurately model hypersonic flow when a thin hypersonic shock layer exists and most of the momentum from the fluid is transferred to redirecting the fluid. Additionally, the MNA model within MFTK also includes surface calculations of velocity, temperature, and streamline length based on tangential velocity vectors and streamline marching. Using the MNA+FPBL model, these streamlines enable one to compute the shear stress and heat flux using a one-dimensional viscous model [13]. To complete an in-depth code-verification analysis, a proper understanding of the equations (shown in Appendix IV) and cases with known solutions are required.

A. Code Verification with Analytical Solutions

Typically, code-verification activities involve verifying differential or integral equations that introduce discretization error into the solution. Because of the simplicity of the MNA model, initial code-verification test cases do not introduce discretization error. Therefore, the relative difference between an exact solution from a separate code and the computed solution from MFTK should be approximately round-off error, such that, if the L^∞-norm

$$\varepsilon_\infty = \max_i \left| \frac{\mathrm{QoI}_{i_{\text{Exact}}} - \mathrm{QoI}_{i_{\text{MFTK}}}}{\mathrm{QoI}_{i_{\text{Exact}}}} \right|, \tag{1}$$

where QoI is the quantity of interest, is less than 10^{-12}, the test passes.

B. Verification Cases

For this analysis, two code-verification cases are studied to identify implementation (also know as constant errors) and meshing errors. Case 1 is a flat-plate case and Case 2 is an inclined-plate case. The flat-plate case is almost identical to inclined-plate case except that the mesh for the inclined-plate case can introduce mesh tolerance errors when inclining the plate. Instead, the flat-plate case inclines the freestream velocity to induce the pressure field since the precision of the freestream velocity is less prone to errors. For both test cases, the following MNA model QoIs are tested: C_p, P_e, $\mathbf{V}_e$, M_e, T_e, ρ_e, $\mathbf{n}_v$, and L. We note that Case 1 and Case 2 do not identify geometry discretization errors, which require order-of-accuracy testing and is left for future work.

1. Case 1: Flat Plate

The flat-plate case models flow over a flat plate, where the angle of attack is $-7°$. The computational domain of the flat-plate case is a 1.0 m by 1.0 m square on the XZ-plane, which is shown in Fig. 1. Since the mesh perfectly represents the geometry and the mesh is aligned with the streamlines, which is shown in Fig. 2, this case uses an analytical solution to test the correct implementation. This case provides the most simplistic MNA model test case to ensure all variables computed by MFTK match the exact solution.

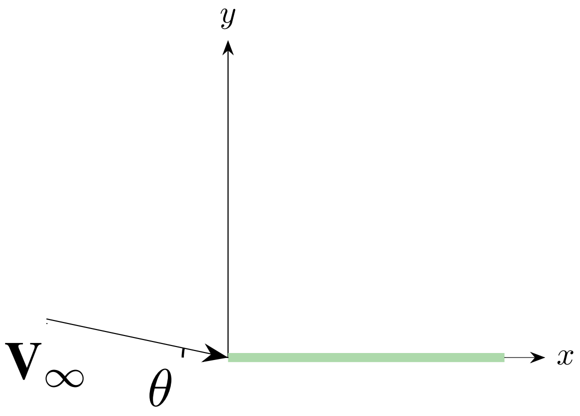

Fig. 1 Computational domain for the flat-plate case (side view).

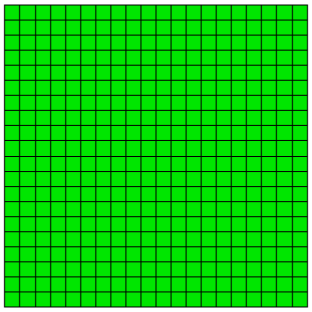

Fig. 2 Coarsest mesh for the flat-plate case (top view).

The exact solution uses the input from Table 3 in conjunction with Eqs (14) through (21) and the velocity specified above. Using Eq (1), the relative error is computed. The results of the code-verification analysis are shown in Table 1.

Table 1 Code-verification results for the flat-plate case.

Variable	Mesh 1 Error	Mesh 2 Error	Mesh 3 Error	Mesh 4 Error
n_x	0.00	0.00	0.00	0.00
n_y	0.00	0.00	0.00	0.00
C_p $[\times 10^{-14}]$	9.67	9.67	9.67	9.67
P $[\times 10^{-14}]$	3.18	3.18	3.18	3.18
u $[\times 10^{-14}]$	5.31	5.31	5.31	5.31
v	0.00	0.00	0.00	0.00
M $[\times 10^{-15}]$	8.14	8.14	8.14	8.14
T $[\times 10^{-15}]$	2.06	2.06	2.06	2.06
ρ $[\times 10^{-14}]$	5.97	5.97	5.97	5.97
Dist $[\times 10^{-16}]$	2.18	2.07	2.07	1.71

All of the errors in the MNA variables are below 10^{-13} and clearly below the test criteria of 10^{-12}, which means the MNA model equations do not have constant errors when the staggered mesh is aligned, which simplifies the streamline calculation. If an implementation error were present, the relative error would be much higher than 10^{-13}, making this verification test quite sensitive to constant errors. One note in completing this verification testing is that precision tolerances are much more important for these tests than realistic problems. This makes setting up the test cases difficult since hidden or rarely used settings can cause issues to the results. We also note that the error in the streamline distance is increasing with mesh refinement. Increasing error is to be expected since round-off error increases with the number of calculations being performed.

2. Case 2: Inclined Plate

The inclined-plate case is identical to the flat-plate case, but the implementation is slightly different. For this case, the velocity is along the x-axis and the plate is inclined by $-7°$, as shown in Fig. 3. Since the mesh perfectly represents the geometry and the mesh is aligned with the streamlines, this case uses an analytical solution to test the correct implementation. This case provides the second most simplistic MNA model test case to ensure all variables computed by MFTK match the exact solution.

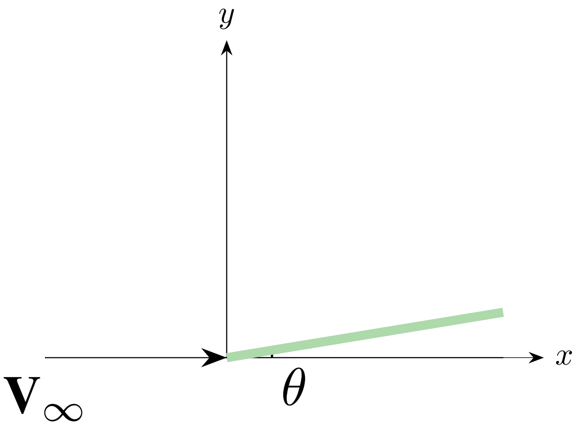

Fig. 3 Computational domain for the inclined-plate case.

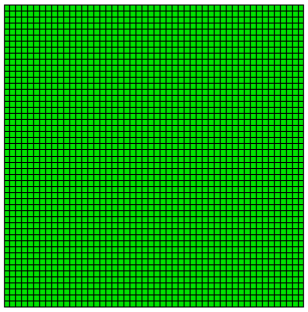

Fig. 4 Coarsest Mesh for the inclined-plate case.

The exact solution uses the input from Table 3 in conjunction with Eqs (14) through (21) and the velocity specified in Section II.B.2. Using Eq (1), the relative error is computed, and the results are shown in Table 2.

All of the errors in the MNA variables are at most $\sim 10^{-13}$ and clearly below the test criteria of 10^{-12}, which means the MNA model equations do not have constant errors when the staggered mesh is aligned, which simplifies the

Table 2 Code Verification Results for the Flat Plate Case

Variable	Mesh 1 Error	Mesh 2 Error	Mesh 3 Error	Mesh 4 Error
n_x $[\times 10^{-13}]$	4.76	4.36	4.35	4.08
n_y $[\times 10^{-14}]$	2.36	2.29	2.26	2.24
C_p $[\times 10^{-13}]$	2.72	2.72	2.72	0.97
P $[\times 10^{-13}]$	1.48	0.84	0.32	0.32
u $[\times 10^{-13}]$	1.55	1.54	1.54	1.54
v $[\times 10^{-13}]$	1.38	0.91	0.47	0.19
M $[\times 10^{-15}]$	8.14	8.14	8.14	8.14
T $[\times 10^{-15}]$	2.06	2.06	2.06	2.06
ρ $[\times 10^{-14}]$	5.97	5.97	5.97	5.97
Dist $[\times 10^{-14}]$	9.51	4.42	1.63	0.92

streamline calculation. One note on this particular problem is that initial results were impacted by the precision of the mesh. This problem requires the maximum precision available from the meshing software to ensure mesh precision does not impact the exact verification results.

3. Coding Error Identified

During the development of Cases 1 and 2, a coding error in how the stagnation point is computed at the edge of a face was identified and corrected. Partial geometry simulations are undertaken to reduce the computational cost of the simulation by utilizing symmetry within the solution. Since partial geometries would have the stagnation point located at the edge of a face, this coding error would have impacted all partial geometry simulations. This finding highlights the importance of completing code verification.

C. Future Work

For future work, an additional test case should also be completed to ensure the MNA model can pass an order-of-accuracy test. One proposed test case would be simulating flow over a blunt-nose cone. This curved geometry would introduce geometry discretization error as well as discretization error from the streamline distance calculation because of the use of an unstructured grid. Additionally, code verification of the FPBL model should be completed for all three test cases. Lastly, code verification should be applied to the momentum/energy integral technique (MEIT) since there is currently no code verification for the implementation within MFTK. Once all these tests have been successfully implemented, these code-verification tests should be automated to ensure MFTK continues to pass these tests with ongoing development.

III. Solution Verification

Once code-verification activities are complete, solution-verification activities can start. Solution-verification activities assess how well discrete equations can approximate the converged solution. This is crucial to complete before validation activities start because the numerical uncertainty can impact the validation assessment. Since the different models in MFTK (MNA, Euler, and RANS) use discrete equations to represent the model, an assessment of the numerical uncertainty needs to be completed for each validation case. For an initial assessment of numerical uncertainty, we will use the GCI metric.

A. GCI Equations

The grid convergence index (GCI) is the most simple and popular method to assess numerical uncertainty. GCI requires solutions on at least three mesh sets (f_1, f_2, and f_3) to compute the observed order of accuracy. The base case developed for the validation study produced a solution on the medium mesh. For this study, a coarser and finer mesh were developed with a uniform refinement (and coarsening) factor of two ($r = 2$)in each direction to generate the additional solutions required. Since the MNA+FPBL model is a panel method, whereas Euler+MEIT and both

RANS models are control-volume methods, two separate mesh triplets were generated. Fig. 5 shows the coarsest 3D surface mesh used for the MNA+FPBL model, whereas Fig. 6 shows the coarsest 2D axisymmetric volume mesh used for the Euler+MEIT and both RANS models. For both meshes, the only significant mesh refinement is near the nose-cone region since large gradients are expected in this region. Each figure focuses on the mesh resolution details in the nose-cone region. The medium and fine cell sizes can resolve length scales approximately two- and four-times smaller than the coarse cell sizes, respectively.

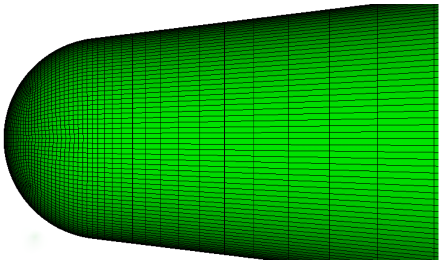

Fig. 5 MNA+FPBL coarse mesh example in nose-cone region.

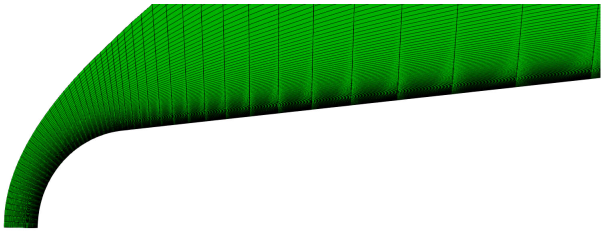

Fig. 6 Euler+MEIT and RANS coarse mesh examples in nose-cone region.

This provides enough information to compute the observed order of accuracy, p_{obs}, which is

$$p_{\text{obs}} = \frac{\ln\left(\frac{f_3-f_2}{f_2-f_1}\right)}{\ln r}. \tag{2}$$

Once we compute the p_{obs}, a factor of safety, F_s, is chosen. This factor of safety turns the discretization error estimate into a 95% confidence interval. Based on [4], when the difference between p_{obs} and the theoretical order of accuracy, p_{th}, is smaller than 10%, $F_s = 1.25$. For all other cases, $F_s = 3.0$. While multiplying the estimated discretization error significantly inflates the reported error, being close to or outside the asymptotic range can negatively impact the quality of the Richardson extrapolation. Additionally, when p_{obs} is positive, but larger in magnitude than p_{th}, it is conservative to use p_{th} in the GCI metric, which will be seen in the order-of-accuracy plots below as a ceiling. When p_{obs} is smaller in magnitude than p_{th}, it is conservative to use p_{obs} in the GCI metric. For the case when p_{obs} is positive, but less than 0.5, the order of accuracy is set to 0.5, which will be seen in the order-of-accuracy plots below as a floor. For the case when p_{obs} is negative, this suggests that the simulation is non-convergent and numerical uncertainty cannot be estimated. Now that F_s and p are known, the GCI metric is computed using

$$\text{GCI} = F_s \frac{|f_3 - f_2|}{(r^p - 1)} \tag{3}$$

B. Solution Verification Assessment

For the solution verification assessment, there are a variety of fidelities and viscous models assessed to match the validation assessment of the HIFiRE-1 wind tunnel test in [14]. To assess the numerical uncertainty for each simulation case, the GCI is computed along the downstream flow. The HIFiRE-1 geometry, shown in Fig. 7, is used for all simulation cases. The model fidelities assessed are MNA+FPBL, Euler+MEIT, and Reynold-averaged Navier–Stokes (RANS) for the 0° angle of attack case. Since the validation assessment is performed on the pressure (P) and wall heat flux (q_w), the solution-verification assessment needs to quantify the numerical uncertainty for those QoIs. In addition to the normalized GCI values, we report simulation results for each level of refinement to quickly assess the mesh sensitivity. Lastly, we also report the observed order of accuracy to show how well the numerical method is performing. For all simulation results, except for the heat flux results from the MNA+FPBL model, the theoretical order of accuracy is assumed to be two, due to the linear approximation of the angle. For the heat-flux results in the MNA+FPBL model, the theoretical order of accuracy is assumed to be one, due to the sub-linear approximation of the streamline distance. To ensure consistently converging results in the future, the streamline distance calculation should be improved to second-order accurate.

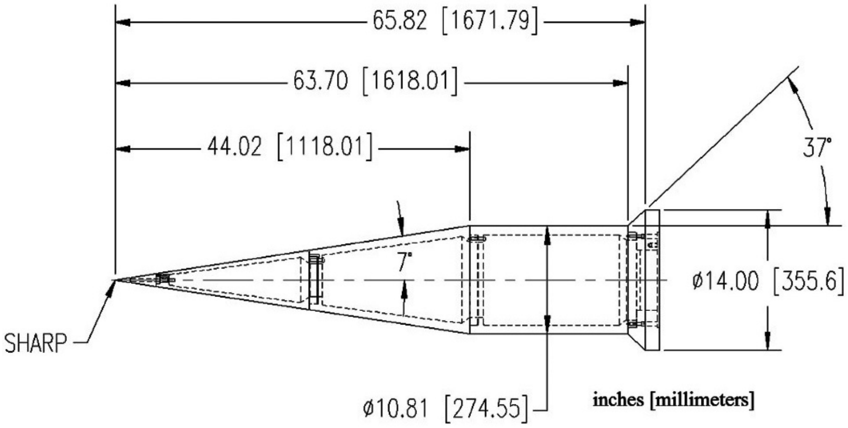

Fig. 7 The HIFiRE-1 wind tunnel test geometry that shows the fore-cone on the left, the cylindrical section in the center, and the flare on the right, from [15]. The text states that the final nosetip was changed from sharp to a radius of 2.5 mm and the flare angle was changed from 37° to 33°.

1. MNA+FPBL with 0° *Angle of Attack*

The MNA+FPBL model with 0° angle of attack case has the option of two different viscous models: flat-plate laminar and flat-plate turbulent using the van Driest model, shown in Figs. 8 and 9. Note that the HIFiRE-1 geometry is shown as a shaded figure in the background of each plot to show the increase in uncertainty due to changes in geometry.

For pressure, both the GCI and order of accuracy perform quite well for the laminar and van Driest cases, except near the discontinuity at the front of the nose cone, which is to be expected. We note that there is a drop in order of accuracy when the angle of the HIFiRE-1 geometry is zero, in the cylindrical portion, since the model is designed to be insensitive when the angle is 0°. For heat flux, the results are less desirable because of the larger sensitivity to the mesh and due to the large variation in order of accuracy, although the numerical uncertainty is still quite small (approximately 3% maximum difference) and the uncertainty and spike in order of accuracy are quite localized. Refinement of the mesh in areas where the angle of the geometry changes should help reduce the increase in numerical uncertainty.

2. Euler+MEIT with 0° *Angle of Attack*

The Euler+MEIT model with the 0° angle of attack case is shown in Fig. 10. This case represents the standard mid-fidelity option within MFTK. Note that the HIFiRE-1 geometry is shown as a shaded figure in the background of each plot to show the increase in uncertainty due to changes in geometry.

For pressure, there are areas in the domain that are not fully resolved with a GCI ratio of up to 3.5. Additionally, the order of accuracy confirms this lack of convergence with spikes from the order of accuracy. For heat flux, rather than modeling the laminar-to-turbulent transition region, MFTK currently switches from laminar to turbulent at $x = 0.45$ m. This is a relatively new addition to MFTK to include both laminar and turbulent solutions. At $x = 0.45$ m, the GCI ratio is up to 10.0, which indicates the manual method of modeling the transition region could use improvement. To improve the transition modeling, the transition model should be adjusted to include a length scale to the transition region to ensure a resolvable transition model. In addition to the transition region, the sharp aft region looks to be under-resolved. If the numerical uncertainty is too large, this could be addressed in future studies by locally refining this region.

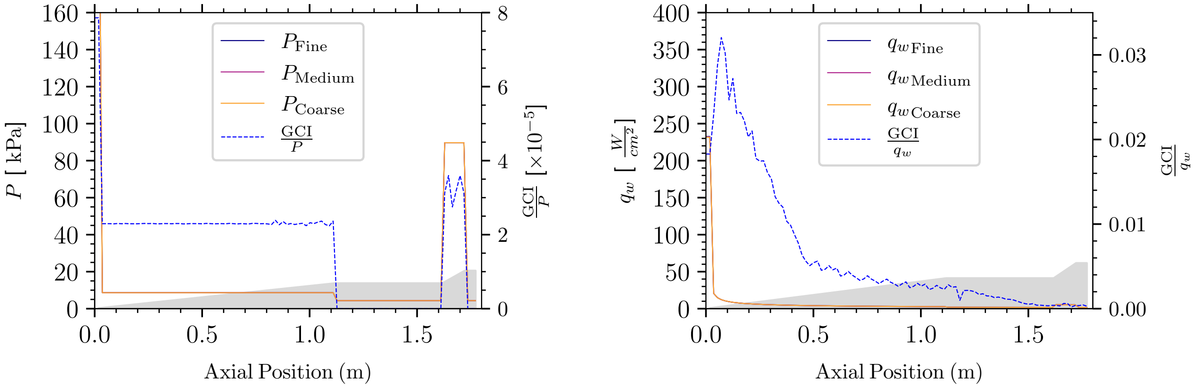

(a) Pressure

(b) Heat flux

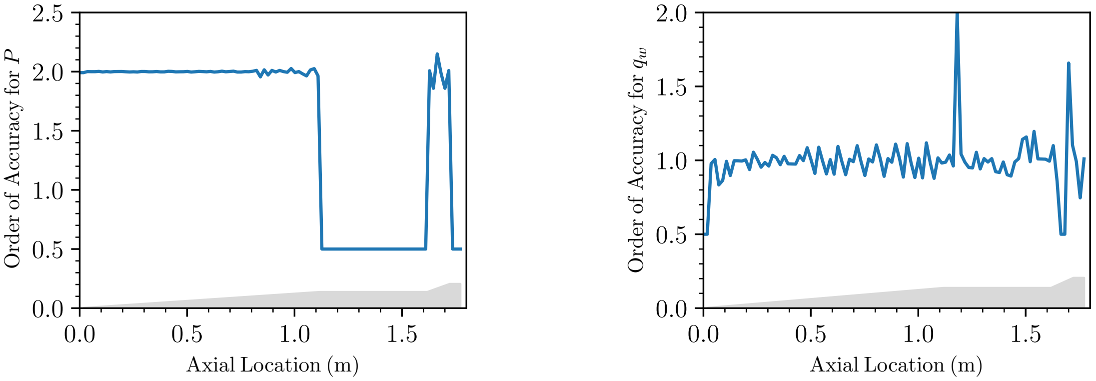

(c) Order of accuracy for pressure

(d) Order of accuracy for heat flux

Fig. 8 GCI calculation for laminar case with 0° angle of attack.

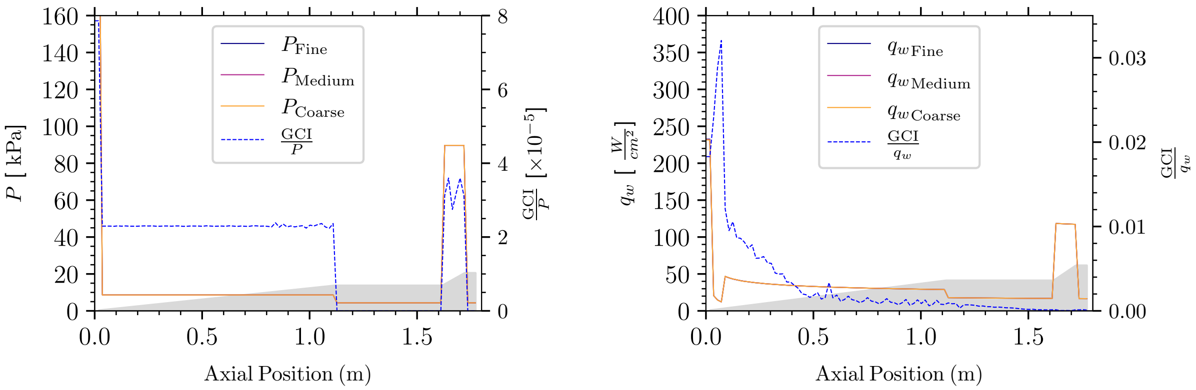

(a) Pressure

(b) Heat flux

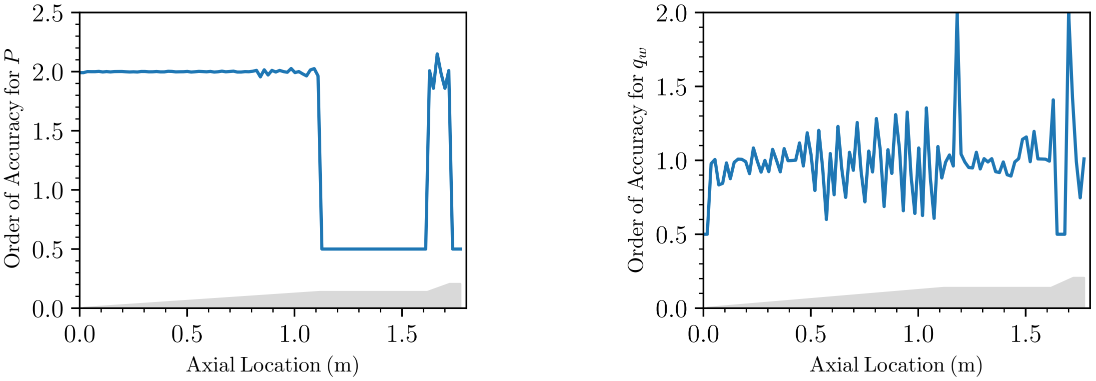

(c) Order of accuracy for pressure

(d) Order of accuracy for heat flux

Fig. 9 GCI calculation for turbulent (Van Driest) case with 0° angle of attack.

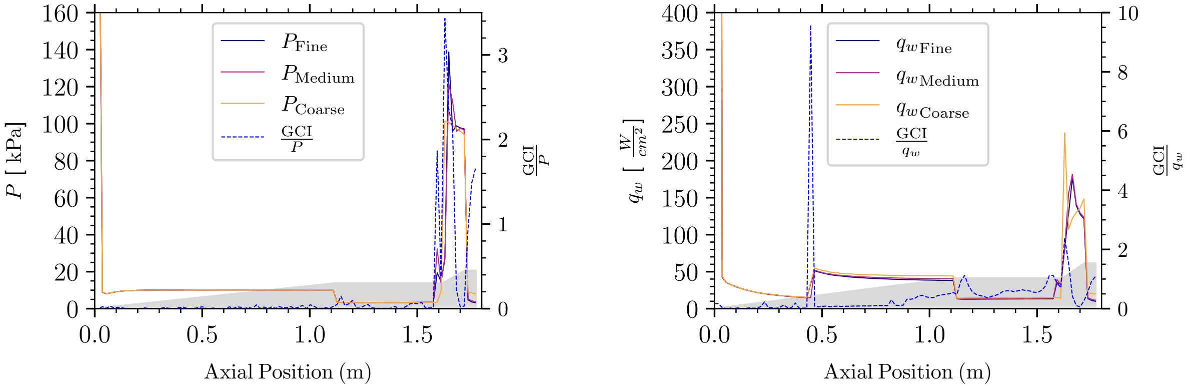

(a) Pressure

(b) Heat flux

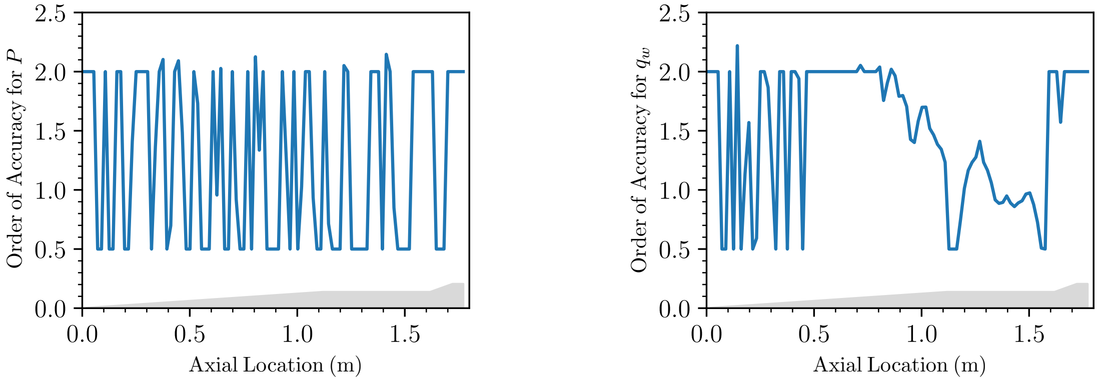

(c) Order of accuracy for pressure

(d) Order of accuracy for heat flux

Fig. 10 GCI calculation for turbulent (MEIT) case with 0° angle of attack.

3. *RANS with 0° Angle of Attack*

The RANS model with 0° angle of attack case has the option of two different viscous models: Spalart–Allmaras (SA) and Shear Stress Transport (SST), shown in Figs. 11 and 12. These cases represent the high-fidelity options within MFTK. Note that the HIFiRE-1 geometry is shown as a shaded figure in the background of each plot to show the increase in uncertainty due to changes in geometry.

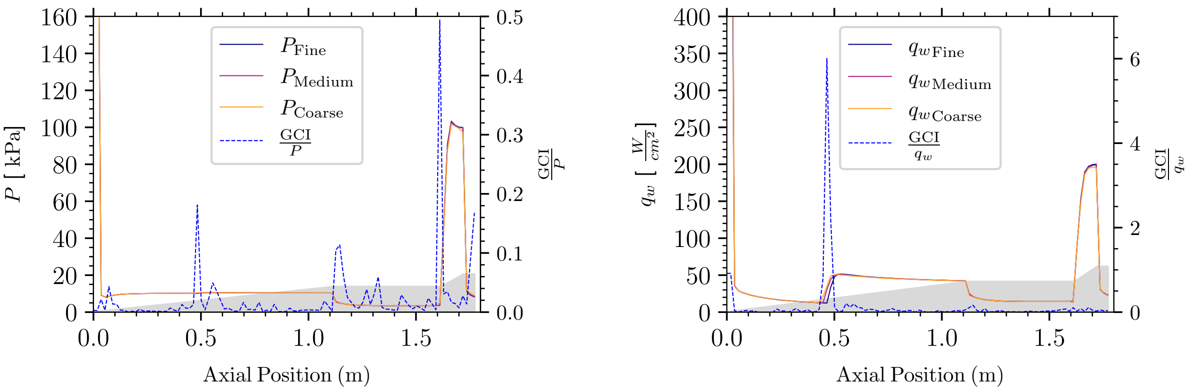

(a) Pressure

(b) Heat flux

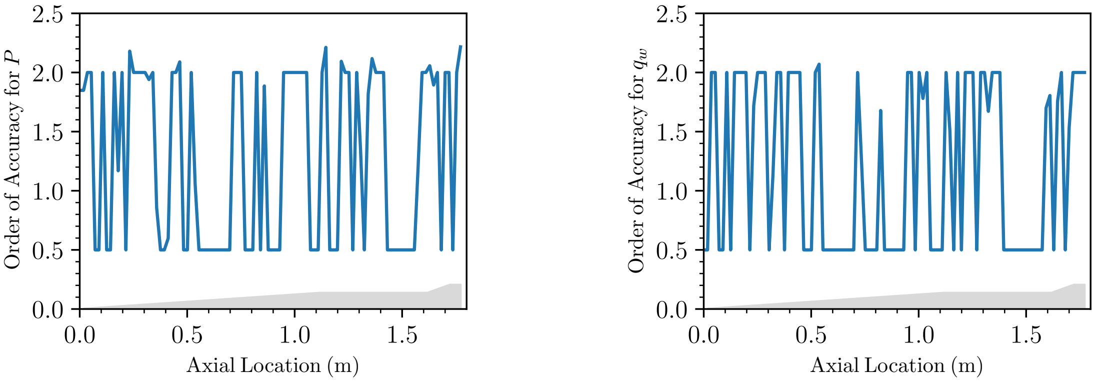

(c) Order of accuracy for pressure

(d) Order of accuracy for heat flux

Fig. 11 GCI calculation for turbulent (SA) case with 0° angle of attack.

For pressure, the GCI and order of accuracy for the SA model performs much better than the SST model, which almost never has an order of accuracy that is close to the theoretical value and a maximum GCI ratio of around 11.0. For heat flux, the results are similar to pressure where the GCI and order of accuracy for the SA model perform much better than the SST model, except for the spike in the GCI ratio near the laminar–turbulent transition region. Regardless of the turbulence model, the chaotic nature of the order of accuracy is concerning and a more refined mesh is probably required unless a large numerical uncertainty is acceptable.

C. Future Work

For future work, additional code verification should be performed for the FPBL, MEIT, and RANS equations to ensure the proper implementation of the models. When reviewing the mid- and high-fidelity numerical uncertainties, the RANS-SA is much lower than the other models. We also point out that even though the RANS-SA model had the lowest numerical uncertainty of the mid- and high-fidelity models, the order of accuracy was sporadic and the GCI value is still quite high. The high GCI value is an important result since these mid- and high-fidelity meshes were considered to be well refined before the analysis was completed. This means that future simulations should use more refined meshes and will unfortunately add to the computational expense, which adds to the appeal of the low-fidelity model. As expected, the low-fidelity MNA+FPBL model's numerical uncertainty is the lowest of all the simulation results. This is due to

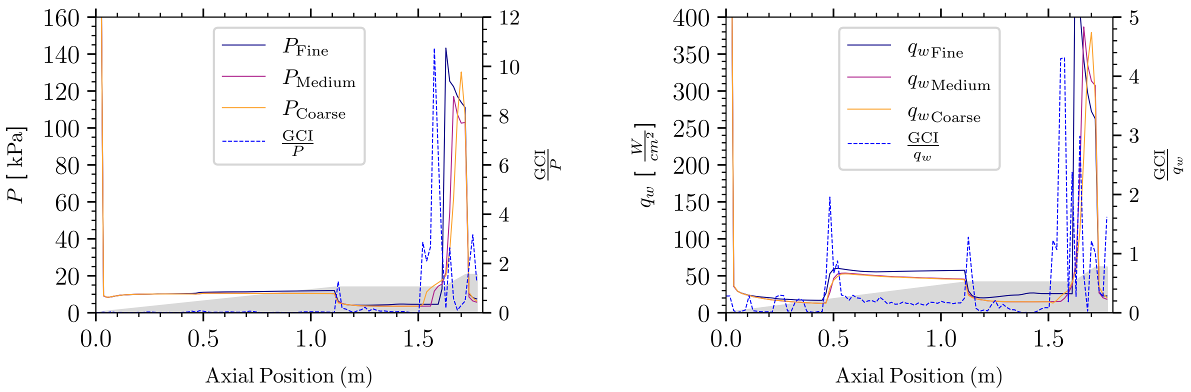

(a) Pressure

(b) Heat flux

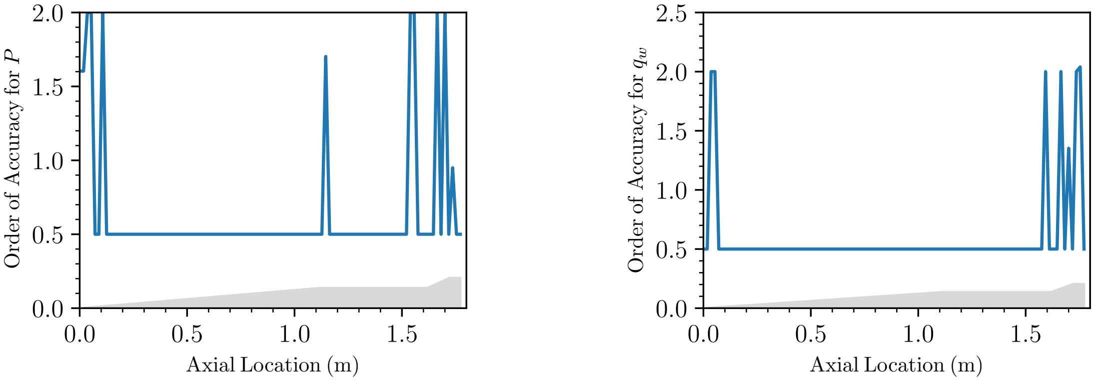

(c) Order of accuracy for pressure

(d) Order of accuracy for heat flux

Fig. 12 GCI Calculation for turbulent (SST) case with 0° angle of attack.

the simplistic nature of the model and reaching well inside the asymptotic region is less computationally expensive. When these cases are evaluated in the validation chapter of this report, results where the GCI ratio is unacceptably high should either be locally or globally refined to ensure the solution is within the asymptotic region. In addition to local and global mesh refinement, the transition from laminar to turbulent solutions should be improved to ensure the transition is smooth. Without a smooth transition, this region is not able to enter the asymptotic range and will yield large numerical uncertainty.

IV. Conclusion

This work undertakes the first known verification activities for the Multi-Fidelity Toolkit to provide credibility evidence for its use in high-consequence decision making in hypersonic vehicle analysis at a variety of physics-fidelity and computational-expense levels. It has leveraged best practices in both code and solution verification. The code-verification activities focused on the modified Newtonian aerodynamics model that is a large component of the low-fidelity capability of MFTK. The other component, the flat-plate boundary layer models, should be the subject of future code-verification efforts. Solution-verification activities were applied to all three fidelity levels of MFTK.

Code and solution verification are vital precursors for high-quality validation activities. By minimizing the coding errors and measuring the numerical uncertainty, we can ensure the impact of discretizing the equations and geometry is minimized. The MNA code-verification results showed that for all QoIs, the difference between the MFTK results and the analytical solution are less than 10^{-13} when the mesh perfectly represents the geometry and the mesh lines up with the streamlines. This means the MNA model has been implemented correctly in MFTK without coding errors for all situations matching the code-verification case scenarios. Additionally, the MNA model has significantly less numerical uncertainty than the Euler-MEIT or either RANS models, which is expected since the asymptotic range for the low fidelity MNA model starts significantly earlier than the Euler-MEIT or either RANS cases. Future Euler-MEIT and RANS-SST cases should be refined where significant numerical uncertainty exists.

Appendix: Derivation of Modified Newtonian Aerodynamics

This appendix focuses on the derivation of the MNA model for inviscid flow regions and the three flat plate boundary layer (FPBL) models for the viscous flow regions.

Assumed Inputs

Before discussing the derivation of the MNA model and the FPBL models, the model inputs should be stated. The following constants are used as inputs into MFTK and will be used as part of the analytic solution. The constant names, notation, and values are listed in Table 3.

Table 3 Table of values used in code-verification analysis.

Constant Name	Notation	Value	Units
Gas constant for air	R	287.05	J/kg/K
Ratio of specific heats	γ	1.4	–
Prandtl number	Pr	0.73684	–
Freestream density	ρ_∞	0.066958	kg/m^3
Freestream speed	V_∞	2170.0	m/s
Freestream velocity	$\mathbf{V}_\infty$	Problem Specific	m/s
Freestream temperature	T_∞	226.46	K
Wall temperature	T_w	300	K
Sutherland constant C	C_{visc}	1.458×10^{-6}	–
Sutherland constant S	S_{visc}	110.3	–

Newtonian Theory

Based on Section 3.2 of [12], Newtonian theory computes the pressure applied by the fluid's momentum in

$$p_e - p_\infty = \rho_\infty V_\infty^2 \sin^2\theta, \tag{4}$$

where p_e is the edge pressure, p_∞ is the freestream pressure shown in

$$p_\infty = \rho_\infty R T_\infty, \tag{5}$$

ρ_∞ is the freestream density, R is the gas constant for air, T_∞ is the freestream temperature, V_∞ is the freestream speed of the flow, and θ is the local surface angle relative to the freestream flow direction. The ratio between the static pressure and the dynamic pressure is C_p and is defined as

$$C_p = \frac{p_e - p_\infty}{\frac{1}{2}\rho_\infty V_\infty^2}. \tag{6}$$

Substituting Eq. (4) into Eq. (7) results in

$$C_p = 2\sin^2\theta. \tag{7}$$

While it is typical to derive these equations on an angled, one-dimensional plate, θ in Eq. (7) is the local angle of the surface. This means that these equations are applicable on two- and three-dimensional surfaces. For complex surfaces, θ is calculated by

$$\theta = \sin^{-1}\left(\frac{\mathbf{V}_\infty}{V_\infty}\cdot\mathbf{n}\right). \tag{8}$$

where $\mathbf{V}_\infty$ is the freestream velocity and **n** is the element surface unit vector. Another important portion of the domain is the other side of the body (also known as the shadow region). Since the shadow region does not undergo the increase in pressure due to the flow, the pressure in the shadow region is the same as p_∞. To account for the shadow region, when $\theta < 0, C_p = 0$.

MNA Model

The MNA model [16] is an improved method to compute the edge pressure distribution, p_e, over blunt-nosed bodies [12]. Additionally, we use p_e to compute edge velocities, $\mathbf{V}_e$, and edge temperatures, T_e. MNA assumes the pressure at the stagnation point is equal to the stagnation pressure behind a normal shock wave (p_{O_2}). This exactly computes C_p at the stagnation point, so it is natural to replace the factor of two in Newtonian theory with a new coefficient. This new coefficient, $C_{p_{\max}}$ is used in the MNA model, such that Eq. (7) becomes

$$C_p = C_{p_{\max}}\sin^2\theta, \tag{9}$$

where

$$C_{p_{\max}} = \frac{p_{\mathrm{O}_2} - p_\infty}{\frac{1}{2}\rho_\infty V_\infty^2}. \tag{10}$$

Noting that $q = \frac{1}{2}\rho_\infty V_\infty^2 = \frac{\gamma}{2}p_\infty M_\infty^2$ (see [12, pg. 44]), Eq. (10) is simplified to

$$C_{p_{\max}} = \frac{2}{\gamma M_\infty^2}\left(\frac{p_{\mathrm{O}_2}}{p_\infty} - 1\right), \tag{11}$$

where γ is the ratio of specific heats and M_∞ is the freestream Mach number and computed using

$$M_\infty = \frac{V_\infty}{\sqrt{\gamma R T_\infty}} \tag{12}$$

Using the Rayleigh pitot tube formula from normal shock-wave theory, the relationship between the total pressure behind the pressure wave compared to the freestream pressure is shown by [12, pg. 65]

$$\frac{p_{\mathrm{O}_2}}{p_\infty} = \left(\frac{(\gamma+1)^2 M_\infty^2}{4\gamma M_\infty^2 - 2(\gamma-1)}\right) \tag{13}$$

By substituting Eq. (11) and Eq. (13) into Eq. (9), the equation is now a function of the ratio of specific heats for air, γ, and M_∞, which matches Eq. (2.3) in [17]. Now that C_p is derived, we can compute p_e by rearranging the terms in Eq. (6) to obtain

$$p_e = \frac{1}{2} C_p \rho_\infty V_\infty^2 + p_\infty \tag{14}$$

Now that p_e has been derived, edge velocity, $\mathbf{V}_e$, and edge temperature, T_e, can be derived. $\mathbf{V}_e$ is defined as

$$\mathbf{V}_e = V_e \cdot \mathbf{n}_v \tag{15}$$

where the edge velocity unit vector, $\mathbf{n}_v$, is computed using the freestream speed of the flow, freestream velocity, and the surface unit vector given by the surface of the body, $\mathbf{n}_s$, in

$$\mathbf{n}_v = \frac{\mathbf{n}_s \times \left(\frac{\mathbf{V}_\infty}{V_\infty}\right)}{\left|\mathbf{n}_s \times \left(\frac{\mathbf{V}_\infty}{V_\infty}\right)\right|}. \tag{16}$$

The edge speed $\mathbf{V}_e$ is computed using the edge Mach number, M_e, (see [12, pg. 79]) and the speed of sound, a in

$$V_e = M_e a, \tag{17}$$

where

$$M_e = \sqrt{\frac{2}{\gamma - 1}\left(\left(\frac{p_e}{p_{e_{\max}}}\right)^{\frac{1-\gamma}{\gamma}} - 1\right)}, \tag{18}$$

$$a = \sqrt{\gamma R T_e}, \tag{19}$$

$$p_{\max} = \frac{1}{2} C_{p_{\max}}, \tag{20}$$

and

$$T_e = T_\infty \frac{1 + \frac{1}{2}\left(\gamma - 1\right) M_\infty^2}{1 + \frac{1}{2}\left(\gamma - 1\right) M_e^2}. \tag{21}$$

Acknowledgments

The authors wish to thank Matthew Bopp, Brian Carnes, and Bryan Morreale for their help in setting up the code-verification cases. The authors also wish to thank Jared Kirsch for his thorough review of the manuscript.

Sandia National Laboratories is a multimission laboratory managed and operated by National Technology & Engineering Solutions of Sandia, LLC, a wholly owned subsidiary of Honeywell International Inc., for the U.S. Department of Energy's National Nuclear Security Administration under contract DE-NA0003525. This paper describes objective technical results and analysis. Any subjective views or opinions that might be expressed in the paper do not necessarily represent the views of the U.S. Department of Energy or the United States Government.

References

[1] Kim, Y., Lee, S., Yee, K., and Rhee, D. H., "High-to-Low Initial Sample Ratio of Hierarchical Kriging for Film Hole Array Optimization," *Journal of Propulsion and Power*, Vol. 34, No. 1, 2018, pp. 108–115. doi: 10.2514/1.B36556.

[2] ASME, "V&V 10-2019: Standard for Verification and Validation in Computational Solid Mechanics," Tech. rep., American Society of Mechanical Engineers, 2020.

[3] Roache, P. J., *Fundamentals of Verification and Validation*, Hermosa publishers, 2009.

[4] Oberkampf, W. L., and Roy, C. J., *Verification and Validation in Scientific Computing*, Cambridge University Press, 2010. doi: 10.1017/cbo9780511760396.

[5] Salari, K., and Knupp, P., "Code Verification by the Method of Manufactured Solutions," Sandia Report SAND2000-1444, Sandia National Laboratories, June 2000. doi: 10.2172/759450.

[6] Freno, B. A., Carnes, B. R., and Weirs, V. G., “Code-Verification Techniques for Hypersonic Reacting Flows in Thermochemical Nonequilibrium,” *Journal of Computational Physics*, Vol. 425, 2021. doi: doi.org/10.1016/j.jcp.2020.1.

[7] Carnes, B. R., Weirs, V. G., and Smith, T., “Code Verification and Numerical Error Estimation for use in Model Validation of Laminar, Hypersonic Double-Cone Flows,” *AIAA Scitech 2019 Forum*, American Institute of Aeronautics and Astronautics, 2019, p. 2175. doi: 10.2514/6.2019-2175.

[8] Roache, P. J., “Perspective: A Method for Uniform Reporting of Grid Refinement Studies,” *Journal of Fluids Engineering*, Vol. 116, No. 3, 1994, pp. 405–413. doi: 10.1115/1.2910291.

[9] Rider, W., Witkowski, W., Kamm, J., and Wildey, T., “Robust Verification Analysis,” *Journal of Computational Physics*, Vol. 307, 2016, pp. 146–163. doi: 10.1016/j.jcp.2015.11.054.

[10] Radtke, G. A., Martin, N., Moore, C. H., Huang, A., and Cartwright, K. L., “Robust Verification of Stochastic Simulation Codes,” *Journal of Computational Physics*, Submitted for Publication.

[11] Eça, L., and Hoekstra, M., “Discretization Uncertainty Estimation Based on a Least-Squares Version of the Grid Convergence Index,” *Proceedings of the Second Workshop on CFD Uncertainty Analysis*, Instituto Superior Tecnico, 2006, pp. 1–27. doi: 10.2514/6.2019-2175.

[12] Anderson Jr, J., *Hypersonic and High-Temperature Gas Dynamics*, American Institute of Aeronautics and Astronautics, 2019. doi: 10.2514/4.861956.

[13] White, F. M., and Corfield, I., *Viscous Fluid Flow*, Vol. 3, McGraw-Hill New York, 2006.

[14] Lance, B. W., Krueger, A. M., Freno, B. A., and Wagnild, R. M., “Validation Studies of the Multi-Fidelity Toolkit,” *AIAA SciTech Forum*, AIAA, Submitted for Publication.

[15] Wadhams, T., Mundy, E., MacLean, M., and Holden, M., “Ground Test Studies of the HIFiRE-1 Transition Experiment Part 1: Experimental Results,” *Journal of Spacecraft and Rockets*, Vol. 45, No. 6, 2008, pp. 1134–1148.

[16] Lees, L., “Hypersonic Flow,” *Journal of Spacecraft and Rockets*, Vol. 40, No. 5, 2003, pp. 400–735.

[17] Wagnild, R. M., Dinzl, D. J., Bopp, M. S., Dement, D. C., Robbins, B. A., Bruner, C. W. S., Grant, M. J., Murray, J., and Harper, J. M., “Development of a Multi-fidelity Toolkit for Rapid Aerothermal Model Development,” Sandia Report SAND2019-13632, Sandia National Laboratories, Oct 2019.